Title: Strain hardening of as-extruded Mg-xZn (x = 1, 2, 3 and 4 wt%) alloys

Authors: Chaoyue Zhao, Xianhua Chen, Fusheng Pan, Jingfeng Wang, Shangyu Gao, Teng Tu, Chunquan Liu, Jiahao Yao, Andrej Atrens

PII: S1005-0302(18)30196-8
DOI: https://doi.org/10.1016/j.jmst.2018.09.015
Reference: JMST 1306

To appear in:

Received date: 8-3-2018
Revised date: 4-6-2018
Accepted date: 20-6-2018

Please cite this article as: Zhao C, Chen X, Pan F, Wang J, Gao S, Tu T, Liu C, Yao J, Atrens A, Strain hardening of as-extruded Mg-xZn (x = 1, 2, 3 and 4 wt%) alloys, *Journal of Materials Science and amp; Technology* (2018), https://doi.org/10.1016/j.jmst.2018.09.015

Strain hardening of as-extruded Mg-*x*Zn (*x* = 1, 2, 3 and 4 wt%) alloys

Chaoyue Zhao[1], Xianhua Chen[1,2*], Fusheng Pan[1,2], Jingfeng Wang[1,2], Shangyu Gao[1], Teng Tu[1] , Chunquan Liu[1], Jiahao Yao[3], Andrej Atrens [4]

[1] International Joint Laboratory for Light Alloys (Ministry of Education), College of Materials Science and Engineering, Chongqing University, Chongqing 400045, China

[2] National Engineering Research Center for Magnesium Alloys, Chongqing University, Chongqing 400045, China

[3] Shenyang National Laboratory for Materials Science, Institute of Metal Research, Chinese Academy of Sciences, Shenyang 110016, China

[4] School of Mechanical and Mining Engineering, The University of Queensland, St Lucia, 4072 Qld, Australia

[Received 8 March 2018; Received in revised form 4 June 2018; Accepted 20 June 2018]

*Corresponding author, E-mail: xhchen@cqu.edu.cn (Xianhua Chen).

The influence of Zn on the strain hardening of as-extruded Mg-*x*Zn (*x* = 1, 2, 3 and 4 wt%) magnesium alloys was investigated using uniaxial tensile tests at 10^{-3} s^{-1} at room temperature. The strain hardening rate, the strain hardening exponent and the hardening capacity were obtained from true plastic stress-strain curves. There were almost no second phases in the as-extruded Mg-Zn magnesium alloys. Average grain sizes of the four as-extruded alloys were about 17.8 μm. With increasing Zn content from 1

to 4 wt%, the strain hardening rate increased from 2850 MPa to 6810 MPa at (σ-$\sigma_{0.2}$) = 60 MPa, the strain hardening exponent n increased from 0.160 to 0.203, and the hardening capacity, Hc increased from 1.17 to 2.34. The difference in strain hardening response of these Mg-Zn alloys might be mainly caused by weaker basal texture and more solute atoms in the α-Mg matrix with higher Zn content.

Keywords： Mg-Zn alloy; Strain hardening; Dislocation; Basal texture

1. Introduction

As the lightest metallic structural metal found in the world today, Mg and its alloys have many superior properties and been widely used in various fields [1-3]. However, because of their limited strength, ductility and formability, extensive application of Mg alloys is strongly limited [4]. It is necessary to further improve the mechanical properties of Mg alloys to expand their range of application [5,6]. Therefore, great attention has been paid lately to the investigation of the influence of alloy elements on microstructures and room-temperature mechanical properties of Mg alloys.

Strain hardening in magnesium alloys is an obvious feature in the process of plastic deformation [7]. It has a great influence on the mechanical properties of alloys. Strain hardening is mainly related to dislocation accumulation and annihilation, and affords resistance to further deformation of metallic materials [8]. Current studies on strain hardening theory are mainly focused on face-centered cubic (fcc) metals, and are based on the accumulation of a forest of dislocations [9,10]. Due to the more complex hardening case, the theory of strain hardening in hexagonal metals has not been well established, especially in magnesium alloys. Toward this end, many authors have studied the strain hardening behavior of magnesium alloys, and taken many aspects into consideration, such as second phase, grain size, texture, twinning,

temperature, and strain rate [11-14]. Jahedi et al. [12] reported that strain hardening was strongly related to twinning and texture. Chen et al. [10] researched strain hardening behaviors of ZK60 alloy after different heat treatments. However, research is still limited into the influence of alloying elements on the straining hardening of magnesium alloys.

In particular, Zn is an effective alloying element that can improve the mechanical properties of magnesium alloys [15-17]. Hence, high strength Mg-Zn alloys have a broad application prospect in many fields [18-21]. However, only limited studies have been reported on the details of the strain hardening behavior of Mg-Zn alloys.

This work investigated the effects of the Zn concentration on the strain hardening response of as-extruded Mg-Zn alloys, by means of tensile testing at room temperature. The results and related discussion provide an important basis for understanding the strain hardening of Mg-Zn alloys and developing new high-performance Mg-Zn alloys for engineering applications.

2. Experimental procedures

Ingots of Mg-Zn binary alloys were prepared from high-purity Mg (99.98 wt%) and Zn (99.99 wt%) using an electric resistance furnace under a mixed protective gas of CO_2 and SF_6. The molten alloys were cast into a cylindrical steel mold, homogenized at 420 °C for 18 h and quenched into water at 25 °C. The chemical compositions of the experimental alloys were determined by X-ray fluorescence spectrometry, and are listed in Table 1. The Mg-Zn alloys are designated as Mg-1Zn, Mg-2Zn, Mg-3Zn and Mg-4Zn. After homogenization, the ingots with a diameter of 80 mm were extruded at 300 °C with an extrusion ratio of 25:1 into cylinder bars with a diameter of 16 mm, by applying a constant force using an XJ-500 Horizontal Extrusion Machine, and a ram speed of 1 m/min. The extruded bars were machined into tensile test rods with a diameter of 5 mm and a gauge length of 25 mm. The tensile tests were carried out at room temperature using a CMT5105 material testing machine at a strain rate of 10^{-3} s^{-1}. The tensile yield strength (YS), ultimate tensile

strength (UTS) and elongation to fracture are average values of at least three individual repeated tests. Microstructures of as-textured Mg-Zn samples were observed using an optical microscope (OM), a JEOL JSM-7800F field emission scanning electron microscope (SEM) equipped with a HKL Chanel 5 electron backscattered diffraction (EBSD) system using a scan step-size of 0.6 mm, and a transmission electron microscope (TEM, Tecnai G2 F20 S-TWIN) with an accelerating voltage of 200 kV, after tensile straining. For OM observation, the polished specimens were etched in a solution of 16 ml of alcohol + 1 g of picric acid + 2.6 ml of glacial acetic acid. 4 mm × 6 mm × 2.5 mm block samples for EBSD observation were electropolished using a solution (of 100 ml isopropanol + 800 ml ethanol + 18.5 ml distilled water + 10 g hydroxyquinoline + 75 g citric acid + 41.5 g sodium thiocyanate + 15 ml perchloric acid) cooled to -30° at 20 V for 90 s. EBSD samples of as-extruded Mg-Zn alloys after uniaxial tensile deformation were obtained from locations nearing the fracture. Thin foil specimens for TEM observation were prepared through mechanical polishing and ion-beam thinning using a Gatan Precision Ion Polishing System at room temperature. Phase analysis was conducted on a Rigaku D / MAX-2500PC X-ray diffractometer (XRD). The average grain size and average Schmid factor were measured using an HKL Chanel 5 System with more than three continuous EBSD data at a magnification of 400 times.

3. Results

3.1. Microstructure characterization

Fig. 1 shows XRD patterns of as-extruded Mg-Zn alloys, indicating that there was essentially no phase detected other than α-Mg. Fig. 2, the optical micrographs of the as-extruded Mg-Zn samples indicates that there was almost no second phase in these alloys. The microstructure of these samples was characterized by relatively-uniform equiaxed grains, indicating that full recrystallization had taken place during the hot extrusion. EDS maps also indicated that Zn atoms were dissolved in matrix and the solubility of Zn atoms increased with increasing Zn content, as

shown in Fig. 3. Because the maximum solubility of Zn element in Mg is 6.2 wt%, no second phase was precipitated during the hot extrusion even for the as-extruded Mg-4Zn samples. Fig. 4(a)-(d) shows the inverse pole figures (IPFs) of the as-extruded samples. The color of the grains represents grain orientation as indicated in Fig. 4(e). During hot extrusion process, dynamic recrystallization (DRX) occurred and significantly refined the grain size. For the extruded alloys, the average grain size was in the range of 17.6-17.9 μm and did not change as the Zn content increased from 1 to 4 wt%, as shown in Fig. 4(f). This result shows that the grain size was not refined with increasing Zn concentration in the α-Mg matrix. Langelier et al. [22] and Ha et al. [23] also reported that the average grain size of as-extruded Mg-Zn alloys was similar and that the Zn alloying was completely dissolved in the α-Mg matrix.

Fig. 5 presents the pole figures of the as-extruded Mg-Zn samples. The {0001} plane of the as-extruded Mg-Zn samples was approximately parallel to the extrusion direction, which is an annular fiber texture, which is also called the basal texture. With increasing Zn concentration from 1 wt% to 4 wt%, the intensity of the basal texture decreased from 12.8 to 8.6, which indicated that an increase of Zn concentration weakened the intensity of the basal texture. Langelier et al. [22] and Wang et al. [24] also reported that the intensity of the basal texture decreased with increasing Zn concentration. Formation of a basal texture is due to the large amount of activated basal plane slip during hot extrusion. Zn could reduce the axial ratio (c/a) value of the magnesium and promote the initiation of non-basal slip, and thereby decrease the intensity of the basal texture [25,26]. The change of the intensity of the basal texture might influence the strain hardening behavior of the as-extruded Mg-Zn alloys.

Fig. 6 shows EBSD maps of as-extruded Mg-Zn samples after tensile fracture. In the IPF maps, grain boundaries marked by black lines are high-angle grain boundaries with misorientation angles larger than 10°, and grain boundaries marked by white lines are low-angle grain boundaries with misorientation angles lower than 10°. The amount of low-angle grain boundaries increased with increasing Zn concentration.

There were $\{10\bar{1}2\}$ tension twins marked by red lines and $\{10\bar{1}1\}$ compression twins marked by green lines in the deformation microstructure. The quantity of deformation twins was small and there was no obvious difference in volume fraction of tension and compression twins in the as-extruded Mg-Zn samples with various Zn concentrations. Because of its lower critical resolved shear stress (CRSS) compared with $\{10\bar{1}1\}$ compression twinning, $\{10\bar{1}2\}$ tension twinning occurs easily during plastic deformation in magnesium alloys [27]. However, the *c*-axis of most grains was approximately perpendicular to the direction of the applied stress due to the basal texture in the as-extruded Mg-Zn samples. Hence, a certain amount of $\{10\bar{1}1\}$ compression twinning occurs during uniaxial tensile straining. Moreover, comparing band contrast maps and IPF maps, there is some lines that are not recognized as twin boundaries or low-angle grain boundaries, which would be traces left by dislocation slip inside grains. It indicates that movement and interaction of dislocations were the major modes for the plastic deformation of the as-extruded Mg-Zn alloys.

Fig. 7 presents the TEM images of the as-extruded Mg-1Zn and Mg-4Zn alloys. The dislocation structure in the as-extruded Mg-4Zn sample was similar to dislocation cells, which are formed by a high-density dislocation area when the dislocation density reaches a certain value. Due to the activation of multiple slip, the dislocation density rapidly increased and the high-density dislocation areas transformed into dislocation cells [28,29]. Therefore, dislocation cell formation requires a sufficiently high dislocation density. Fig. 7(a) shows that, compared with the Mg-4Zn sample, the structure of dislocation cells in Mg-1Zn was not obvious. The dislocation density in Mg-1Zn was not high enough to form relatively obvious dislocation cells. Hence, the difference in dislocation structures might affect the strain hardening response of the as-extruded Mg-Zn specimens.

3.2. Strain hardening behavior

Fig. 8(a) presents typical engineering tensile stress–strain curves for the four

alloys. With increasing Zn concentration from 1 wt% to 4 wt%, the tensile strength of the as-extruded samples increased from 226 MPa to 248 MPa, the elongation increased from 16.2% to 21.2%, and the yield strength decreased from 150 MPa to 134 MPa. The enhancement of elongation and the decrease of the yield strength might be influenced by the decreased basal texture intensity with increasing Zn content [30,31]. The increase of tensile strength is considered to be related to the enhanced strain hardening ability.

Based on the relatively uniform deformation, these engineering curves can be converted to true stress–strain curves. Conversion standard formula assumes that the total volume did not change and that the area of cross-section along the gauge length was uniform during the deformation. True stress–strain curves are presented in Fig. 8(b). Corresponding true tensile properties including σ_{UTS}, $\sigma_{0.2}$ and ε_p are summarized in Table 2.

The strain hardening behavior of the as-extruded Mg-Zn alloys is analyzed using the strain hardening rate θ, defined as [32]:

$$\theta = \mathrm{d}\sigma/\mathrm{d}\varepsilon \quad (1)$$

where σ and ε are the macroscopic true stress and true plastic strain, respectively. Fig. 9(a) presents the strain-hardening rate θ vs net flow stress (σ-$\sigma_{0.2}$) curves and Fig. 9(b) shows the strain-hardening rate θ vs true plastic strain ε_p curves for the as-extruded Mg-Zn samples with various Zn concentrations. Fig. 9(a) shows that the strain hardening rate θ increased from 2850 MPa to 6810 MPa at (σ-$\sigma_{0.2}$) = 60 MPa with increasing Zn content. Moreover, because of a short elastoplastic transition, the as-extruded Mg-Zn alloys showed a sharp hardening decrease at the beginning of curves, and then an almost linearly decrease. The stage of the linearly decrease is similar to the well-known stage III strain hardening in fcc polycrystals, beginning at $\theta \approx 4500$ MPa. Thereafter, in the as-extruded Mg-3Zn and Mg-4Zn samples, the pace of strain hardening rate decline slowed down gradually, which was similar to stage IV strain hardening in fcc polycrystals. Fig. 9(b) shows a similar change compared to Fig. 9(a). These curves are decreasing rapidly and almost overlapping with each other at the beginning, which was also due to the short elastoplastic transition. Then the

falling pace of strain hardening rate slowed down at $\varepsilon_p \approx 3\%$.

The hardening capacity, Hc, of a material can be described by the ratio of (σ_{UTS} - $\sigma_{0.2}$) to $\sigma_{0.2}$ [33]:

$$Hc = (\sigma_{UTS} - \sigma_{0.2}) / \sigma_{0.2} \quad (2)$$

Based on the definition of Eq. (2), the hardening capacity of these alloys is shown in Table 2. The value of Hc increased from 1.17 to 2.34 with increasing Zn concentration from 1 to 4 wt% in the as-extruded Mg-Zn alloys. Since grain size did not show significant changes, the variation of Hc may be related to dislocation movement in the as-extruded Mg-Zn alloys.

For the cause of further quantifying strain hardening behavior of as-extruded Mg-Zn alloys, the uniform plastic deformation stage in the uniaxial tensile curve is fitted by the equation [34]:

$$\sigma = K\varepsilon_p^n \quad (3)$$

where K is strength coefficient, and n is the strain hardening exponent. The strain hardening exponent n characterizes condition of necking, which is equal to (or approximately equal to) the size of the maximum uniform strain of a material in an uniaxial tension test. It actually reflects the strain homogenization ability of a material. Fitting results for the as-extruded Mg-Zn samples are listed in Table 2. The value of n increased from 0.160 to 0.203 with increasing Zn concentration: n was intimately dependent on the Zn concentration.

4. Discussion

Generally speaking, slip means dislocation movement and carries plastic deformation. The process of plastic deformation closely relates to changes of dislocation density and dislocation movement, and affects the strain hardening behavior. The strain hardening behavior in metallic material occurs because of dislocation interaction. Original dislocation tangling would hinder further movement of other dislocations. Considering the effects of grain size and dislocations, a recent model indicates that [10-14, 35]:

$$\sigma = \sigma_0 + \sigma_{HP} + \sigma_d \quad (4)$$

where σ_0 is a frictional contribution, $\sigma_{HP} = kd^{-1/2}$ is the Hall–Petch contribution and $\sigma_d = M\eta Gb\rho^{1/2}$ is the Taylor dislocation contribution; where ρ is the dislocation density, η is a constant, M is Taylor factor, G is shear modulus; and b is Burgers vector. Using the Hall–Petch formula $\sigma_{0.2} = \sigma_0 + kd^{-1/2}$, Eq. (4) can be converted into:

$$\sigma \approx \sigma_{0.2} + \sigma_d \quad (5)$$

The stress contribution related to the dislocation density can be obtained by subtracting the yield stress $\sigma_{0.2}$ from the total flow stress as:

$$\rho^{1/2} \propto \sigma_d \approx (\sigma - \sigma_{0.2}) \quad (6)$$

The result of the formula deduction shows that the net flow stress (σ-$\sigma_{0.2}$) of a material is proportional to the dislocation density. Since there is no significant change in grain size, the factors that influence dislocation behaviors inside grains (such as texture intensity and solute atoms) might influence the strain hardening response and need to be considered.

4.1 Rate of dislocation storage in the as-extruded Mg-Zn alloys

Fig. 9(a) shows that these curves of strain hardening rate θ vs (σ-$\sigma_{0.2}$) are almost parallel to each other before (σ-$\sigma_{0.2}$) = 140 MPa at room temperature. It means that dynamic recovery, associated with the slope, is almost the same as stage III [35,36]. The strain hardening behavior related to dislocations might be influenced by dislocation accumulation at least in stage III. θ_0^{III} is a hardening limit extrapolated to (σ-$\sigma_{0.2}$) = 0 to represent the value of stage III strain hardening.

With increasing Zn concentration from 1 to 4 wt%, θ_0^{III} increased from 4355 MPa to 5373 MPa. Whereafter, in Mg-3Zn and Mg-4Zn, when (σ-$\sigma_{0.2}$) ≥ 140 MPa, the pace of strain hardening rate decline slowed down gradually, which is similar to stage IV strain hardening in fcc polycrystals. Fig. 7 shows that, compared with Mg-1Zn, Mg-4Zn had more obvious dislocation cells, whose formation requires a sufficiently high dislocation density. Activation of non-basal slip in magnesium alloys can form

forest of dislocations and increase the dislocation density effectively. The existence of dislocation cells means that there is a relatively high dislocation density in this alloy [28]. Furthermore, in stage IV strain hardening, active dislocations could be continuously absorbed by the boundaries of dislocation cells [29]. Dislocation cells would convert to sub-boundaries (low-angle grain boundaries) when they absorbed enough mobile dislocations. As shown in Fig. 6, the amount of low-angle grain boundaries marked by white lines, increased with increasing Zn concentration, which also indicated the occurrence of stage IV. To some extent, the formation of a subboundary alleviates the softening effect due to dynamic recovery [37,38]. Hence, the decline pace of strain hardening rate slows down obviously in Mg-3Zn and Mg-4Zn. Stage IV strain hardening occurs when the true strain of Mg-3Zn and Mg-4Zn reaches by about 16%. In some fcc polycrystals, when the grain size was about 20 μm, stage IV strain hardening occurred at a true strain of 12%-18% [39,40]. In the end, the alloys are about to break and leading to a rapid hardening decrease at the final part of curves in as-extruded Mg-3Zn and Mg-4Zn.

In the Kocks strain hardening model [31], the relationship between the rate of dislocation storage and ρ is as follows:

$$\mathrm{d}\rho/\mathrm{d}\gamma = k + k_1\rho^{1/2} - k_2\rho \quad (7)$$

where $k = (bd)^{-1}$ describes the athermal storage of dislocations at grain boundaries determined by grain size. The term $k_1\rho^{1/2}$ is associated with a statistical storage of dislocations (also athermal) and the term $-k_2\rho$ is associated with dynamic recovery.

Based on rate of dislocation storage, the microscopic hardening rate could be obtained as follows:

$$\theta = \mathrm{d}\tau/\mathrm{d}\gamma = (\alpha\mu b/2\rho^{1/2}) \times (\mathrm{d}\rho/\mathrm{d}\gamma) \quad (8)$$

Many authors [41,42] think that the well-fitted theoretical model at small scales could be smoothly and simply analogized to the next larger scale. Eqs. (6) and (8) indicate that the relationship of $(\sigma\text{-}\sigma_{0.2})\theta$ vs $(\sigma\text{-}\sigma_{0.2})$ is equivalent to that of $\mathrm{d}\rho/\mathrm{d}\gamma$ vs $\rho^{1/2}$. From Fig. 10, the relationship between the rate of dislocation storage $\mathrm{d}\rho/\mathrm{d}\gamma$ and the dislocation density $\rho^{1/2}$ can be obtained. Eq. (7) shows that the first part of these curves can be fitted with straight lines through the origin. The slope of these straight

lines would be strongly affected by the grain size. Because of the same grain size in these as-extruded alloys, the first part of the four curves has almost the same slope θ_0. After a short elastoplastic transition, stage III strain hardening occurs and shows near parabolic curves in agreement with the relationship in Eq. (7). In this stage, since dynamic recovery is almost the same with increasing Zn content, the increase of dislocation storage is mainly due to the increase of dislocation accumulation. Moreover, when (σ-$\sigma_{0.2}$) $\geq$ 140 MPa, in Mg-3Zn and Mg-4Zn, the formation of sub-boundary alleviates softening effect caused by dynamic recovery, due to occurrence of stage IV strain hardening. This leads to more dislocation storage in Mg-3Zn and Mg-4Zn.

4.2 Influence of basal texture on dislocation storage

Various texture intensity values can change the critical resolved shear stress on basal and non-basal planes. Different textures can change the Schmid factor for basal and non-basal slips, and have thereby an effect on the activation of slip systems.

In the as-extruded Mg-Zn alloys, the measured values of σ and ε can be related to the resolved shear stress τ, and the shear strain γ, on the basal planes by the relations [36]:

$$\varepsilon = m_{\mathrm{s,b}}\gamma \quad (9)$$

$$\sigma = \tau/m_{\mathrm{s,b}} \quad (10)$$

where $m_{\mathrm{s,b}}$ is the Schmid factor for basal slip, $m_{\mathrm{s,b}} = \cos\lambda - \cos\psi$ (where λ and ψ are angles between the stress axis and the slip direction and the slip plane normal, respectively).

The CRSS on basal planes is [36]:

$$\tau_{\mathrm{basal}} = m_{\mathrm{s,b}} \times \sigma_{0.2} \quad (11)$$

In the early stages of deformation, plastic deformation is mainly carried by basal slip in the as-extruded Mg-Zn alloys. Nevertheless, stage III strain hardening is closely related to multiple slip. In order to supplement the deformation in the *c*-axis, multiple slip operated. As the beginning of multiple slip, stage III strain hardening

occurs after the elastoplastic transition, beyond a flow stress close to 170 MPa, 169 MPa, 164 MPa and 162 MPa, respectively. The CRSS on prismatic planes can be obtained as follows [14, 36]:

$$\tau_{\text{prism}} = m_{\text{s,p}} \times \sigma \quad (12)$$

$$\tau_{<c+a>} = m_{<c+a>} \times \sigma \quad (13)$$

where $m_{\text{s,p}}$ is the Schmid factor for prismatic slip, and $m_{<c+a>}$ is the Schmid factor for <*c*+*a*> second order slip on pyramidal planes.

Since the intensity of basal texture of the as-extruded Mg-Zn alloys decreased with increasing Zn content, the average Schmid factor for basal slip increased and that for multiple slip decreased. τ_{basal}, τ_{prism} and $\tau_{<c+a>}$ of the as-extruded Mg-Zn alloys can also be acquired, as shown in Table 3. The values of $\tau_{\text{prism}}/\tau_{\text{basal}}$ and $\tau_{<c+a>}/\tau_{\text{basal}}$, which can change dislocation activity, decrease with increasing Zn content. The value of $\tau_{\text{non-basal}}/\tau_{\text{basal}}$ could reflect the difficulty of non-basal slip operation[43]. Multiple slip would be easier to operate with a lower value of $\tau_{\text{non-basal}}/\tau_{\text{basal}}$ [44]. Forest dislocations are the dominant hardening mechanism [10]. Activation of non-basal slip would promote dislocation interactions and accumulate forest dislocations. Therefore, a decrease of $\tau_{\text{prism}}/\tau_{\text{basal}}$ and $\tau_{<c+a>}/\tau_{\text{basal}}$ with increasing Zn content is beneficial to multiple slip and causes the increase of dislocation storage in as-extruded Mg-Zn alloys.

4.3 Influence of solute atom on dislocation storage

The solute atom also had an influence on strain hardening behavior in as-extruded Mg-Zn alloys. As shown in Fig. 3, with increasing Zn content, more Zn atoms are dissolved and disturbed uniformly in α-Mg matrix. Because Zn can reduce the axial ratio (*c*/*a*) value of magnesium and improve lattice symmetry, non-basal slip would be initiated easier in magnesium alloys at room temperature. Akhtar et al. [45,46] added Zn into magnesium alloys and found that Zn could increase the CRSS on the basal plane and reduce CRSS on the prism plane at the same time. Decrease of the axial ratio (c/a) value also caused the reduction of basal texture intensity in

as-extruded alloys, as indicated in Fig.5.

As is mentioned about, increasing Zn content would reduce the axial ratio (c/a) value of magnesium significantly and then decrease the value of $\tau_{non\text{-}basal}/\tau_{basal}$ [47,48]. Lower value of $\tau_{non\text{-}basal}/\tau_{basal}$ is benefit to activation of non-basal slip, enhances ductility of the alloys and then promotes the dislocation storage in as-extruded Mg-Zn alloys. As shown in Fig. 9, for as-extruded Mg-3Zn and Mg-4Zn, more solute Zn atoms significantly increased non-basal slip and promoted occurrence of stage IV strain hardening, which was confirmed in Figs. 6 and 7. Therefore, more solute Zn atoms in α-Mg matrix are favorable to the improvement of the strain hardening ability in the as-extruded Mg-Zn alloys.

5. Conclusions

The effect of Zn on the strain hardening response of extruded Mg-*x*Zn (*x* = 1, 2, 3 and 4 wt%) magnesium alloys was investigated using uniaxial tensile tests at room temperature. The conclusions are as follows:

(1) The grain size did change and the intensity of basal texture decreased with increasing Zn content from 1 to 4 wt% in the as-extruded Mg-Zn alloys.

(2) Zn addition leads to an obvious increase in strain hardening ability of the as-extruded Mg-Zn alloys. With increasing Zn content from 1 to 4 wt%, the strain hardening rate increases significantly, the strain hardening exponent *n* increases from 0.160 to 0.203, and the hardening capacity Hc is enhanced from 1.17 to 2.34.

(3) The variation of strain hardening behavior of the as-extruded Mg-Zn samples with different Zn contents could be interpreted by texture and solute influences. The weaker basal texture and more Zn solute atoms are able to promote initiation of non-basal slip in magnesium alloys at room temperature and lead to a higher rate of dislocation storage.

Acknowledgments

This work was financially supported by the National Key R&D Program of China (No. 2016YFB0301100), the National Natural Science Foundation of China (Nos. 51571043 and 51531002), and the Fundamental Research Funds for the Central Universities (No. 2018CDJDCL0019).

References

[1] S.H. You, Y.D. Huang, K.U. Kainer, N. Hort, J. Magnes. Alloys 5 (2017) 239-253.

[2] F.S. Pan, M.B. Yang, X.H. Chen, J. Mater. Sci. Technol. 32 (2016) 1211-1221.

[3] X.J. Wang, D.K. Xu, R.Z. Wu, X.B. Chen, Q.M. Peng, L. Jin, Y.C. Xin, Z.Q. Zhang, Y. Liu, X.H. Chen, J. Mater. Sci. Technol. 34 (2018) 245-247.

[4] F.S. Pan, X.H. Chen, T. Yan, T.T. Liu, J.J. Mao, W. Luo, Q. Wang, J. Peng, A.T. Tang, B. Jiang, J. Magnes. Alloys 4 (2016) 8-14.

[5] H. Liu, H. Huang, X.W. Yang, C. Li, J.L. Yan, J.H. Jiang and A.B. Ma, J. Magnes. Alloys 5 (2017) 231-237.

[6] X.Y Xu, X.H. Chen, W.W. Du, Y.X. Geng, F.S. Pan. J. Mater. Sci. Technol. 33 (2017) 926-934.

[7] J. Koike, T. Kobayashi, T. Mukai, H. Watanabe, M. Suzuki, K. Maruyama, K. Higashi, Acta Mater. 51 (2003) 2055-2065.

[8] R. Maaß, S. V. Petegem, D.C. Ma, J. Zimmermann, D. Grolimund, F. Roters, H. V. Swygenhoven, D. Raabe, Acta Mater. 57 (2009) 5996-6005.

[9] M.X. Yang, F.P. Yuan, Q.G. Xie, Y.D. Wang, E. Ma, X.L. Wu, Acta Mater. 109 (2016) 213-222.

[10] X.H. Chen, F.S. Pan, J.J. Mao, J.F. Wang, D.F. Zhang, A.T. Tang, J. Peng, Mater. Des. 32 (2011) 1526-1530.

[11] K. Shiraishi, T. Mayama, M. Yamasaki, Y. Kawamura, Mater. Sci. Eng. A 672 (2016) 49-58.

[12] M. Jahedi, B. A. McWilliams, P. Moy, M. Knezevic, Acta Mater. 131 (2017) 221-232.

[13] X.Z. Lin, D.L. Chen, J. Mater. Eng. Perform. 17 (2008) 894-901.

[14] C. Y. Zhao, X.H. Chen, F.S. Pan, S.Y. Gao, D. Zhao, X.F. Liu, Mater. Sci. Eng. A

713 (2018) 244-252.

[15]F. Wang, T. Hu, Y.T. Zhang, W.L. Xiao, C.L. Ma, Mater. Sci. Eng. A 704 (2017) 57-65.

[16]R.Q. Zhang, J.F. Wang, S. Huang, S.J. Liu, F.S. Pan, J. Magnes. Alloys 5 (2017) 355-361.

[17]C. Xiao, L.Q. Wang, Y.P. Ren, S.N. Sun, E.L. Zhang, C.N. Yan, Q. Liu, X.G. Sun, F.Y. Shou, J.Z. Duan, H. Wang, G.W. Qin, J. Mater. Sci. Technol. 34 (2018) 1618-1627.

[18]M. Rashad, F.S. Pan, Y.L. Liu, X.H. Chen, H. Lin, R.J. Pan, M. Asif, J. She, J. Magnes. Alloys 4 (2016) 270-277.

[19]S.Z. Zhu, T.J. Luo, Y.S. Yang, J. Mater. Sci. Technol. 33 (2017) 1249-1254.

[20]P. Liu, H.T. Jiang, Z.X. Cai, Q. Kang, Y. Zhang, J. Magnes. Alloys 4 (2016) 188-196.

[21]Y.S. Yi, Y. Meng, D.Q. Li, S. Sugiyama, J. Yanagimoto, J. Mater. Sci. Technol. 34 (2018) 1149-1161.

[22]B. Langelier, A.M. Nasiri, S.Y. Lee, M.A, Mater. Sci. Eng. A 620 (2015) 76-84.

[23]H.Y. Ha, J.Y. Kang, J. Yang, C.D. Yim, B.S. You, Corros. Sci. 75 (2013) 426–433.

[24]G.G. Wang, G.S. Huang, X. Chen, Q.Y. Deng, A.T. Tang, B. Jiang, F.S. Pan, Mater. Sci. Eng. A 705 (2017) 46-54.

[25]Y. Chino, M. Kado, M. Mabuchi, Acta Mater. 56 (2008) 387–394.

[26]Y. Chino, M. Kado, M. Mabuchi, Mater. Sci. Eng. A 494 (2008) 343–349.

[27]Y. Liu, N. Li, M. A. Kumar, S. Pathak, J. Wang, R.J. McCabe, N.A. Mara , C.N. Tome, Acta Mater. 135 (2017) 411-421.

[28]A. Seeger, H. Kronmüller, S. Mader, H. Träuble, Philos. Mag. 6 (1961) 639-655.

[29]C.S. Lei, X.T. Deng, X.L. Li, Z.D. Wang, G.D. Wang, R.D.K. Misra, J. Alloys Compd. 689 (2016) 718-725.

[30]M. Kavyani, G. R. Ebrahimi, M. Sanjari, M. Haghshenas, J. Magnes. Alloys 4 (2016) 89-98.

[31]Q Li, G. J. Huang, X. D. Huang, S. W. Pan, C. L. Tan and Q. Liu, J. Magnes. Alloys 5 (2017) 166-172.

[32]U.F. Kocks, H. Mecking, Prog. Mater. Sci. 48 (2003) 171-273.

[33]T.T. Liu, F.S. Pan, X.Y. Zhang, Mater. Des. 43 (2013) 572-577.

[34]D.D. Zhang, D.P. Zhang, F.Q. Bu, X.L. Li, B.S. Li, T.L. Yan, K. Guan. Q. Yang, X.J. Liu, J. Meng, J. Alloys Compd. 728 (2017) 404-412.

[35]J. Balík, P. Dobroň, F. Chmelík, R. Kužel, D. Drozdenko, J. Bohlen, D. Letzig, P. Lukáč, Int. J. Plast. 76 (2015) 166-185.

[36]J.A.D. Valle, F. Carreño, O.A. Ruano, Acta Mater. 54 (2006) 4247-4259.

[37]S. Vafaeian, A. Fattah-alhosseini, Y. Mazaheri, M.K. Keshavarz, Mater. Sci. Eng. 669 (2016) 480-489.

[38]S.O. Gashti, A. Fattah-alhosseini, Y. Mazaheri, M.K. Keshavarz, J. Alloys Compd. 658 (2016) 854-861.

[39]S. Kang, J.G. Jung, M. Kang, W. Woo, Y.K. Lee, Mater. Sci. Eng. A 652 (2016) 212-220.

[40]A. Ghatei Kalashami, A. Kermanpur, E. Ghassemali, A. Najafizadeh, Y. Mazaheri, Mater. Sci. Eng. A 678 (2016) 215-226.

[41]W.W. Xu, L. P. Dávila, Mater. Sci. Eng. A 710 (2018) 413-418.

[42]Y.Wang, H. Choo, Acta Mater. 81 (2014) 83-97.

[43]V. Herrera-Solaz, P. Hidalgo-Manrique, M.T. Pérez-Prado, D. Letzig, J. Llorca, J. Segurado, Mater. Lett. 128 (2014) 199-203.

[44]L. Wang, Z. Zheng, H. Phukan, P. Kenesei, J.-S. Park , J. Lind, R.M. Suter, T.R. Bieler, Acta Mater. 132 (2017) 598-610.

[45]A. Akhtar, E. Teghtsoonian, Acta Metall. 17(1969) 1339-1349.

[46]A. Akhtar, E. Teghtsoonian, Acta Metall. 17 (1969) 1351-1356.

[47]S. Ganeshan , S.L. Shang, Y. Wang, Z.K. Liu, Acta Mater. 57 (2009) 3876-3884.

[48]L. Wang, Y.Q. Zhao, J. Zhang, R. Ma, Y.D. Liu, Y.N. Wang, Q. Zhang, W.G. Li, Y. Zhang, J. Mater. Sci. Technol. 2018, in Press, https://doi.org/10.1016/j.jmst.2018.02.011.

Table list:

Table 1. Chemical compositions of the Mg-Zn alloys (wt%).

Alloy	Mg-1Zn	Mg-2Zn	Mg-3Zn	Mg-4Zn
Design composition	1	2	3	4
Actual composition	1.00	2.16	3.13	3.99

Table 2. Yield strength ($\sigma_{0.2}$), ultimate tensile strength (σ_{UTS}), elongation-to-failure (ε_f), uniform strain (ε_p), hardening capacity (Hc) and strain hardening exponent (n) of the as-extruded Mg-Zn specimens.

Alloy	σ_{UTS} (MPa)	$\sigma_{0.2}$ (MPa)	ε_f (%)	ε_p (%)	Hc	n
Mg-1Zn	254	116	16.2	14.9	1.17	0.160
Mg-2Zn	258	109	16.4	15.2	1.36	0.164
Mg-3Zn	276	98	18.5	17.0	1.81	0.183
Mg-4Zn	297	89	20.6	19.1	2.34	0.203

Table 3. Parameters for dislocation slip systems of the as-extruded Mg-Zn alloys.

Alloy	Basal <*a*>		Prism <*a*>		<*c*+*a*> Second order		$\tau_{prism}/\tau_{basal}$	$\tau_{<c+a>}/\tau_{basal}$
	$m_{s,b}$	τ_{basal}	$m_{s,p}$	τ_{prism}	$m_{<c+a>}$	$\tau_{<c+a>}$		
Mg-1Zn	0.16	18.5	0.45	76.5	0.43	73.1	4.1	3.9
Mg-2Zn	0.17	18.5	0.44	74.8	0.42	70.1	4.0	3.8
Mg-3Zn	0.19	18.6	0.44	72.1	0.41	67.2	3.9	3.6
Mg-4Zn	0.21	18.7	0.43	69.6	0.39	63.2	3.7	3.4

Figure List

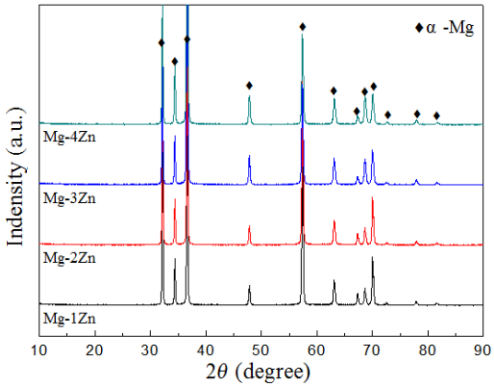

Fig. 1. XRD patterns of as-extruded Mg-Zn alloys

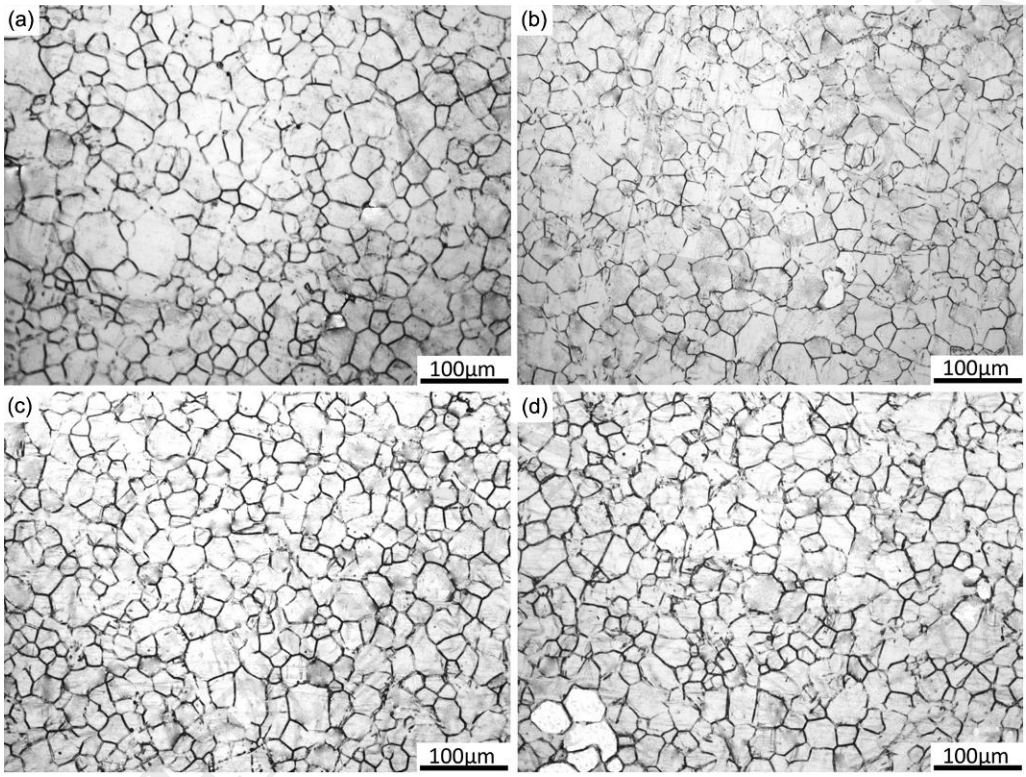

Fig. 2. Optical micrographs of asextruded Mg-Zn alloys: (a) Mg-1Zn, (b) Mg-2Zn, (c) Mg-3Zn, (d) Mg-4Zn.

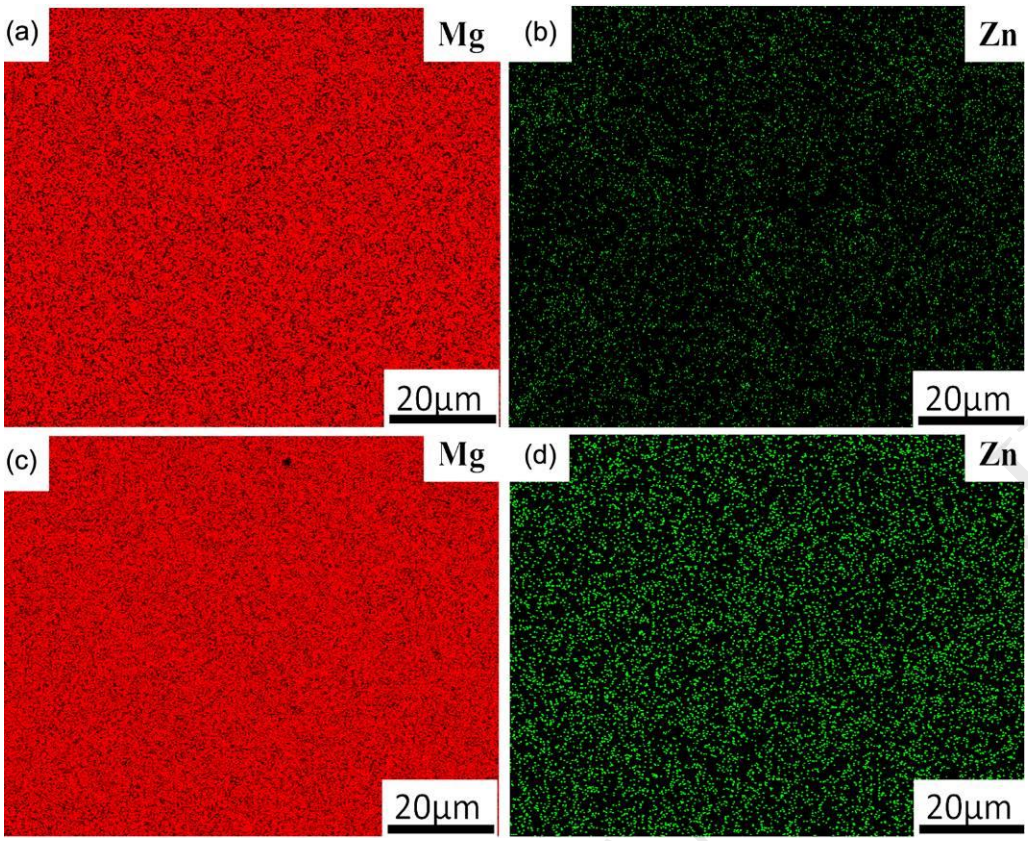

Fig. 3. EDS maps of as-extruded Mg-Zn samples: (a, b) Mg-1Zn, (c, d) Mg-4Zn.

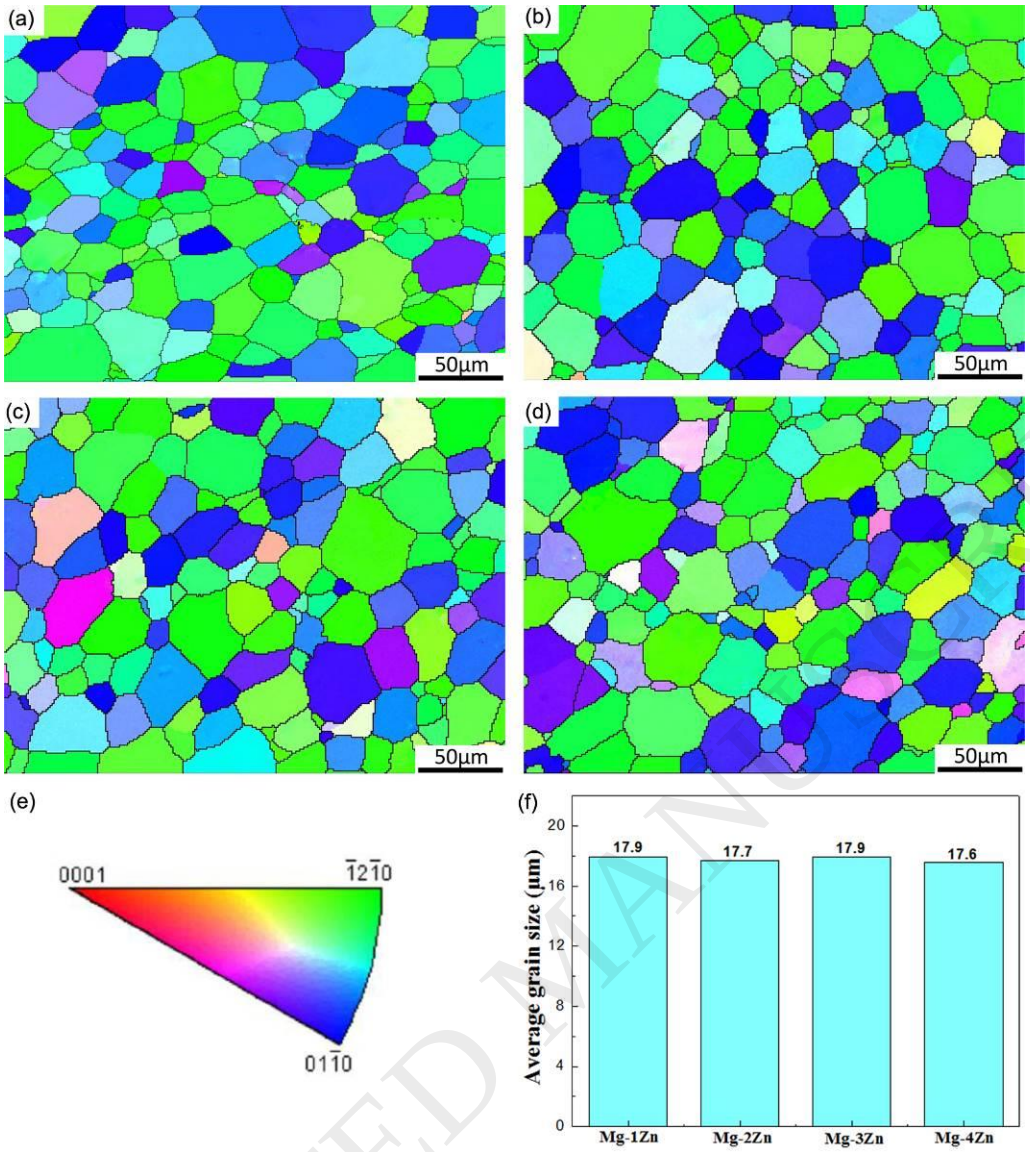

Fig. 4. IPF maps and average grain size of as-extruded Mg-Zn alloys: (a) Mg-1Zn, (b) Mg-2Zn, (c) Mg-3Zn, (d) Mg-4Zn, (e) legend of IPF map, (f) average grain size.

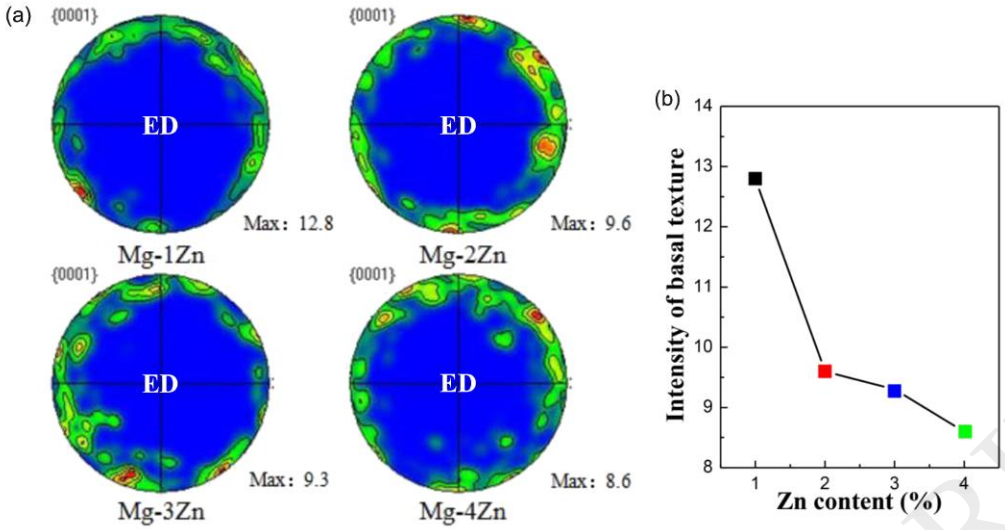

Fig. 5. (a) Pole figures of as-extruded Mg-Zn alloys, (b) variation of intensity of basal texture with different Zn content.

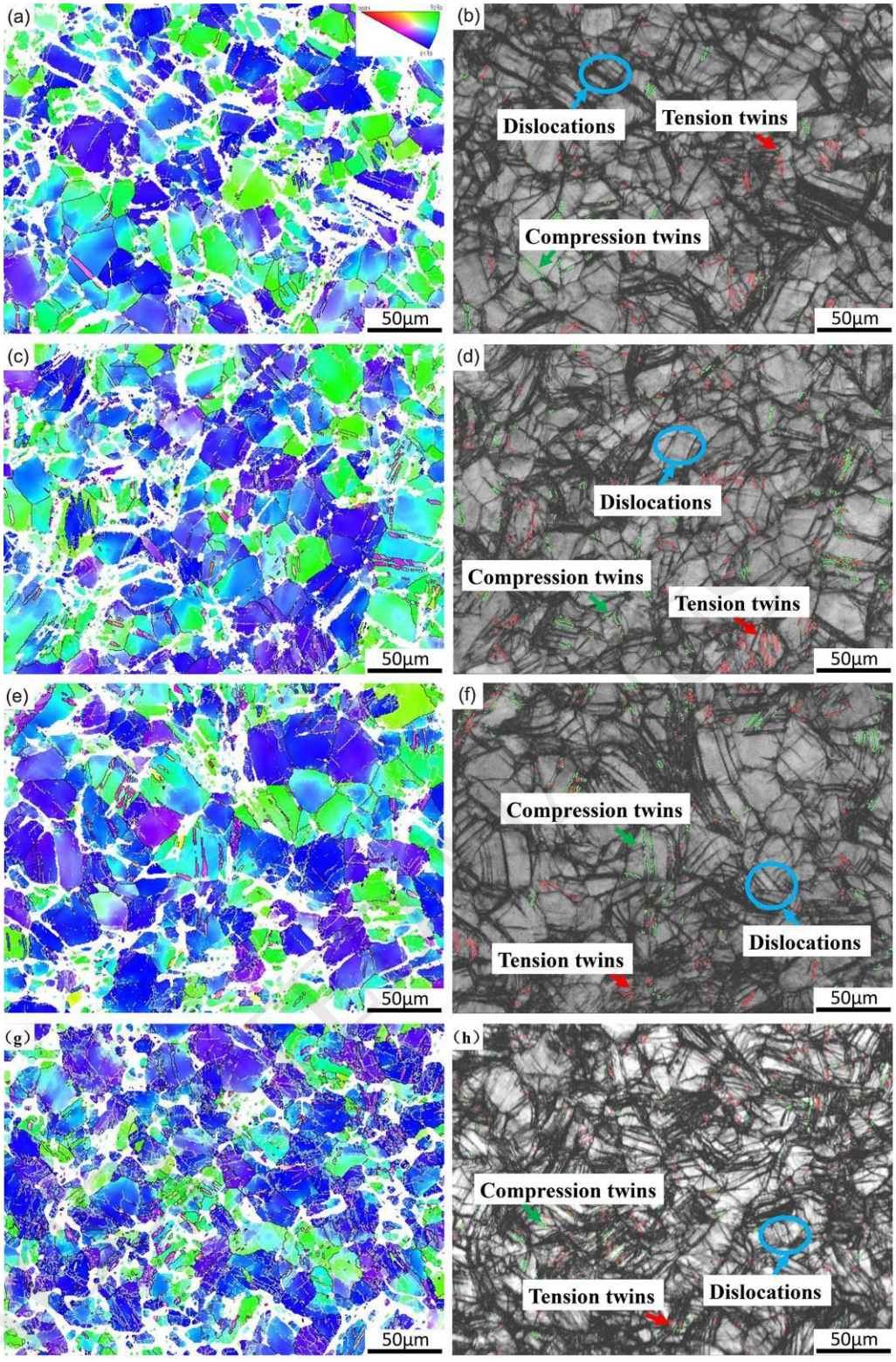

Fig. 6. EBSD maps of as-extruded Mg-Zn samples after tensile fracture: IPF maps of Mg-1Zn (a), Mg-2Zn (c), Mg-3Zn (e) and Mg-4Zn (g); band contrast maps of Mg-1Zn (b), Mg-2Zn (d), Mg-3Zn (f) and Mg-4Zn (h).

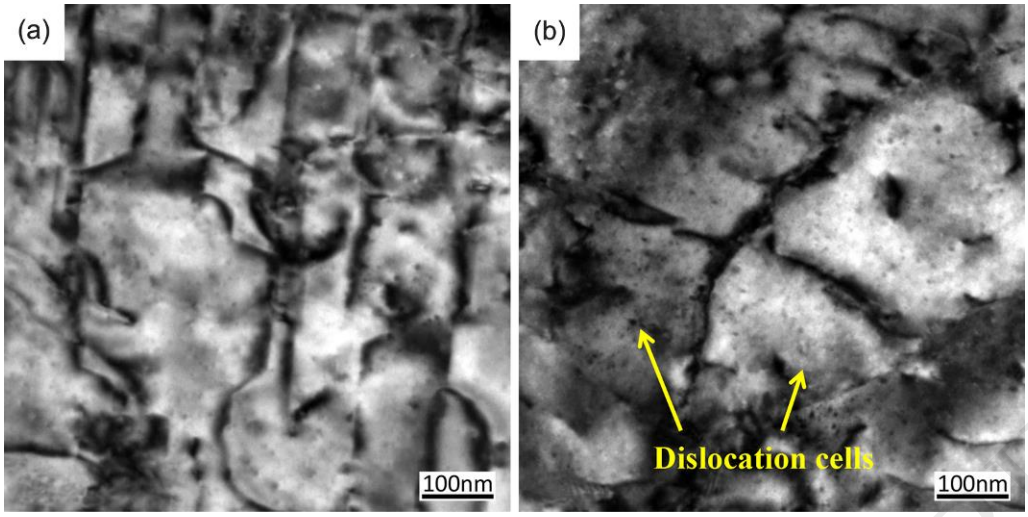

Fig. 7. TEM images of as-extruded Mg-Zn alloys: (a) Mg-1Zn, (b) Mg-4Zn.

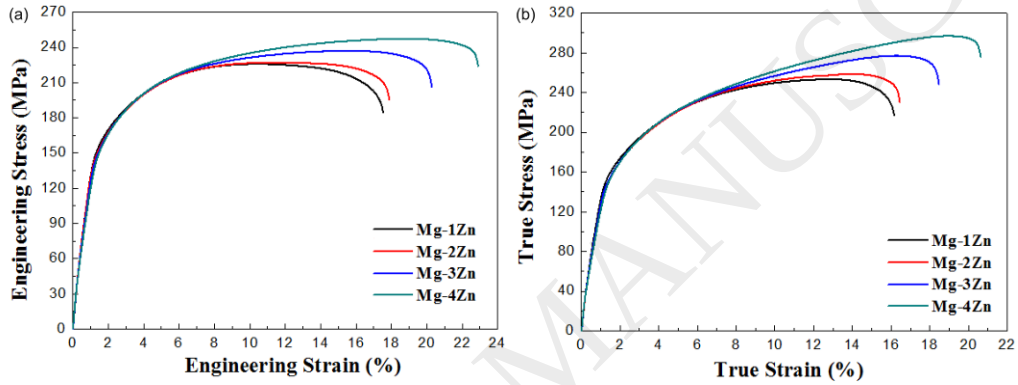

Fig. 8. Engineering (a) and true (b) stress–strain curves for as-extruded samples.

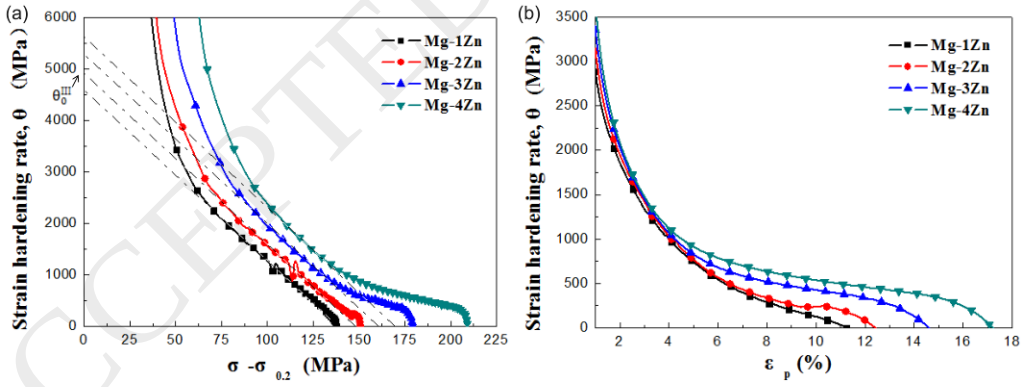

Fig. 9. Strain-hardening curves for as-extruded samples: (a) θ–(σ-$\sigma_{0.2}$), (b) θ–ε_p.

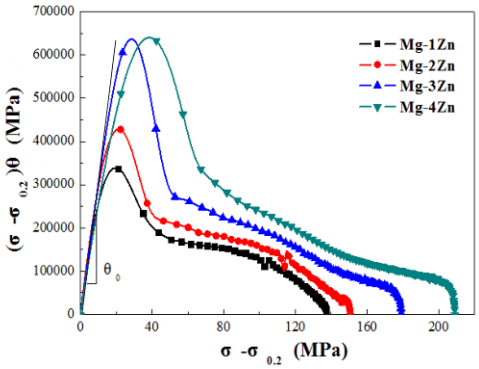

Fig. 10. Relationship between $(\sigma-\sigma_{0.2})\theta$ and $(\sigma-\sigma_{0.2})$ for as-extruded Mg-Zn alloys.